Large tandem duplications in cancer result from transcription and DNA replication collision

Yang Yang[1], Michelle L. Badura[2,3], Patrick O'Leary[2], Troy M. Robinson[2,3], Emily A. Egusa[2,3], Xiaoming Zhong[1], Jason T. Swinderman[2,3], Haolong Li[2,3], Meng Zhang[2,3], Minkyu Kim[2,4], Alan Ashworth[2,5], Felix Y. Feng[2,3,5], Jonathan Chou[2,5,**], Lixing Yang[1,6,7,**]

1. Ben May Department for Cancer Research, University of Chicago, Chicago, IL, USA
2. Helen Diller Family Comprehensive Cancer Center, University of California, San Francisco, CA, USA
3. Departments of Radiation Oncology and Urology, University of California, San Francisco, CA, USA
4. Department of Cellular Molecular Pharmacology, University of California San Francisco, San Francisco, CA, USA
5. Division of Hematology/Oncology, Department of Medicine, University of California, San Francisco, CA, USA
6. Department of Human Genetics, University of Chicago, Chicago, IL, USA
7. University of Chicago Comprehensive Cancer Center, Chicago, IL, USA

** correspondence: lixingyang@uchicago.edu, jonathan.chou@ucsf.edu

Abstract

Despite the abundance of somatic structural variations (SVs) in cancer, the underlying molecular mechanisms of their formation remain unclear. Here, we use 6,193 whole-genome sequenced tumors to study the contributions of transcription and DNA replication collisions to genome instability. After deconvoluting robust SV signatures in three independent pan-cancer cohorts, we detect transcription-dependent replicated-strand bias, the expected footprint of transcription-replication collision (TRC), in large tandem duplications (TDs). Large TDs are abundant in female-enriched, upper gastrointestinal tract and prostate cancers. They are associated with poor patient survival and mutations in *TP53*, *CDK12*, and *SPOP*. Upon inactivating or suppressing *CDK12*, cells display significantly more TRCs and R-loops. Inhibition of WEE1, a cell cycle regulator that promotes DNA repair, selectively inhibits the growth of cells with loss of CDK12. Our data suggest that large TDs in cancer form due to TRC, and their presence can be used as a biomarker for prognosis and treatment.

Introduction

Genome instability is a hallmark of cancer. Somatic structural variations (SVs) are abundant in human cancers, especially in solid tumors [1,2]. However, our knowledge of their underlying causes is rather limited. In breast, ovarian, prostate, and pancreatic cancers, small deletions and small tandem duplications (TDs) can be attributed to homologous recombination deficiency (HRD) caused by *BRCA1* or *BRCA2* mutations [3,4]. In lymphoid cells, translocations can result from aberrant V(D)J recombination [5,6]. Many other tumor types also have numerous somatic SVs [2], but their causes remain unclear. The molecular mechanisms underlying genome instability are of clinical significance. For example, individuals carrying germline *BRCA* mutations are at higher risks of breast and ovarian cancers, so it is recommended that cancer screening begins between the ages of 25-35 [7]. More importantly, the genes and pathways associated with the formation of somatic SVs may be druggable. For example, cancers with HRD can be effectively treated by PARP inhibitors [8,9].

DNA replication stress is a major source of genome instability [10,11]. The various types of stress include deregulated origin firing, shortage of nucleotides/proteins, and stalled replication forks. Many studies have demonstrated that the activation of oncogenes, such as Ras, Myc, Mos, and Cyclin E, can promote replication stress, induce collapsed replication forks, and lead to DNA double strand breaks (DSBs) and SVs [12–17]. Here, we focus on the collision between transcription and DNA replication machineries, which is unavoidable because both processes use the same DNA template (**Fig. 1a**). Unresolved head-on collisions result in an accumulation of R-loops, which form DNA breaks [18]. If not repaired properly, the collision may lead to replication fork collapse and genome instability [19]. Some very large genes associated with common fragile sites are hotspots for deletions due to transcription-replication collision (TRC) [20]. Deletions, insertions and point mutations can frequently form when TRCs are induced in a bacterial system [21]. Furthermore, a recent study using population sequencing data revealed transcription- and replication-dependent mutational processes in the human germline [22]. However, the roles of TRCs in genome instability in human cancers remain largely unknown. Moreover, identifying tumors with high levels of TRCs may be clinically actionable, since drugs targeting transcription [23,24], replication [25] and DNA damage repair [26] are available.

Here, we used a total of 6,193 whole-genome sequenced tumors to perform detailed analysis on somatic SVs. We revealed that large TDs result from TRCs and tumor cells with elevated TRCs can be selectively killed by a WEE1 inhibitor.

Results

Simple SV signatures in human cancers

Non-negative-matrix-factorization-(NMF)-based mutational signature decomposition is very effective in extracting signatures and inferring the underlying molecular mechanisms for somatic single nucleotide variants (SNVs) [27,28], copy number variations (CNVs) [29,30], SVs [2,4] and chromosomal instability [31]. Recently, we have discovered six complex SV signatures in the Pan-Cancer Analysis of Whole Genomes (PCAWG) cohort and identified one signature related to circular extrachromosomal DNA (ecDNA) displaying bias in TRC regions [32]. In the current study, we focus on TRCs in simple SVs.

We hypothesized that a subset of somatic simple SVs in cancer result from improperly repaired TRCs. Since NMF-based signatures can robustly capture molecular mechanisms, we used three large-scale cancer whole-genome sequencing (WGS) cohorts to reliably infer simple SV signatures: the PCAWG cohort (2,583 primary tumors across 39 tumor types) [33], the Hartwig Medical Foundation cohort (Hartwig cohort thereafter, 2,367 metastatic tumors across 36 tumor types) [34] and the Personalized OncoGenomics cohort (POG570, 570 metastatic tumors across 26 tumor types) [35] (**Supplementary Table S1**). With a combined set of 5,520 tumors, our study is the largest pan-cancer SV signature study in human cancer to date to the best of our knowledge. In these three cohorts, there were a total of 1,025,587 somatic SVs (288,417 in PCAWG, 668,492 in Hartwig and 68,678 in POG570). Previously, 12 SV signatures were identified in the PCAWG study [2], of which some complex SVs (i.e., chromothripsis) were excluded while other complex SVs (e.g., chromoplexy, cycle of templated insertions, chain of templated insertions, etc.) were included. Therefore, the previous PCAWG SV signatures were a mixture of simple and complex SVs. We have shown that complex SVs form via distinct mechanisms [32]. Hence, to better capture the simple SV (deletions, TDs, inversions and translocations) signatures, all types of complex SVs were excluded in our current study. As a result, there were 133,718, 303,905, and 41,014 simple SVs in the PCAWG, Hartwig and POG570 cohorts, respectively. To better resolve the effect of SV size, we divided both deletions and TDs into 18 different size categories (**Fig. 1b** and Methods). All simple SVs were classified into 49 categories based on SV type and size, and SigProfilerExtractor [36] was used to deconvolute SV signatures. A total of 13 signatures were detected in the PCAWG cohort (**Fig. 1b** and **Supplementary Fig. S1**). There were four signatures of deletions and another four of TDs, as well as fragile site SVs, foldback inversions, unbalanced inversions, large mixed SVs (including large deletions, large TDs, reciprocal inversions and reciprocal translocations) and unbalanced translocations. The deletion and TD signatures were named as “Del1” to “Del4” and “TD1” to “TD4” (**Fig. 1b**). Three of our four TD signatures (TD1, TD3 and TD4) corresponded to Group 1, 2, and 3 tandem duplicator phenotypes in a previous study [37]. In the Hartwig cohort, we identified 14 signatures (**Fig. 1c** and **Supplementary Fig. S2**) which were very similar to the PCAWG signatures (**Fig. 1b**). There were two additional signatures of very small deletions and very small TDs, namely “Del0” and “TD0”, which were likely due to the differences in SV detection algorithms. In the Hartwig cohort, the unbalanced inversions were captured by both foldback inversion and large mixed SV signatures rather than as a standalone signature in the PCAWG cohort (**Fig. 1b** and **1c**). In the

POG570 cohort, the signatures (**Supplementary Fig. S3**) were also consistent with the PCAWG and Hartwig cohorts. In all three cohorts, reciprocal inversions and reciprocal translocations were captured by one signature, which suggested that they may form through a common molecular mechanism. In contrast, unbalanced inversions and unbalanced translocations were captured by distinct signatures, which suggested that they were generated via distinct mechanisms. Interestingly, in all three cohorts, a small fraction of the reciprocal inversions were captured by the large deletion signature Del4 (**Fig. 1b**, **1c** and **Supplementary Fig. S3a**), indicating possible shared molecular mechanisms.

The samples of the PCAWG, Hartwig and POG570 cohorts were collected, processed, and sequenced at different facilities in different countries. Somatic SVs were called by different teams using different algorithms. The simple SV signatures deconvoluted from the three cohorts were highly reproducible. Therefore, our robust SV signatures represented mutational processes of simple SVs in cancer, did not include any complex SVs, and offered better resolution in SV size than the previous study [2]. In the remainder of this study, we mapped simple SVs in primary tumors from additional cohorts to the 13 PCAWG signatures and simple SVs from metastatic tumors to the 14 Hartwig signatures.

SV strand bias in transcription-replication collision regions

Here, we aim to identify SVs generated by improper repair of TRCs. The formation of these SVs should depend on both transcription and DNA replication. It was shown that different SVs have different biases with regard to replication timing [2]. That is, deletions are enriched in early replicated regions whereas other SVs are mainly enriched in late replicated regions. In addition, some SVs are enriched in transcribed genes [38] (**Supplementary Fig. S4a** and **S4b**). However, which SVs result from TRCs remains unclear. The conflicts between transcription and DNA replication can be resolved properly in normal cells by various DNA damage response pathways, such as the Fanconi Anemia pathway [19], which allows DNA replication to progress without error. If the collisions are not properly repaired, however, the collapsed replication forks can eventually lead to SVs (**Fig. 1a**). Importantly, these SVs will bear unique genetic footprints. First, the resulting SV breakpoints should be located in genes. Furthermore, when the replication fork collapses after TRC, one side of the collapsed site has been replicated, whereas the other side remains unreplicated. Such dosage imbalance will lead to strand bias [39] of the resulting SVs. Thus, the replicated strand should be enriched in the SV junctions (**Fig. 1a**).

For each SV breakpoint, two partner DNA fragments are linked together. Each partner has an orientation, typically annotated as “+” or “-” to indicate whether the upstream or the downstream portion of the DNA is linked to its partner. Deletions have “+-” orientations whereas TDs have “-+” orientations (**Supplementary Fig. S5**). To detect the aforementioned SV strand bias, we first defined conserved replication orientations for all protein-coding genes using repli-seq data from 14 cell lines derived from solid tissues (**Fig. 2a** and **Supplementary Fig. S6**). We then randomly shuffled all observed SVs in the tumors and tested for strand bias in simple SVs in the PCAWG and Hartwig cohorts with at least one breakpoint falling in protein-coding genes. By comparing

observed SVs against the randomly shuffled ones, we found that the breakpoints of TD3 and TD4 were consistently enriched in the replicated strand in both cohorts (**Fig. 2b** and **2c**). Large TDs (TD3 and TD4) were abundant in female-enriched cancers (uterus, ovarian, and breast cancers), upper gastrointestinal tract cancers (esophageal and stomach cancers), prostate, and urothelial cancers (**Fig. 2d** and **2e**). Large TDs were also abundant in metastatic head and neck cancers, which include parts of the upper digestive tract as well (**Fig. 2e**). In breast cancer, basal and HER2+ subtypes carried more large TDs than luminal A and B subtypes (**Supplementary Fig. S7**). Using replication orientations determined from the breast cancer cell line MCF7 and the liver cancer cell line HepG2, the strand bias could be observed in TD3 and TD4 in four independent breast cancer cohorts (PCAWG, Hartwig, POG570 and BRCA-EU) and liver cancer (**Fig. 3a** and **3b**). TD3 and TD4 also displayed strand bias in three independent ovarian cancer cohorts (PCAWG, Hartwig and OV-AU) (**Fig. 3c and 3d**), metastatic prostate, and esophageal cancers (**Fig. 3d**).

If large TDs result from TRCs, we expect the strand bias to depend on gene expression. In unexpressed genes, we did not observe strand bias in TD3 or TD4 in the PCAWG and Hartwig cohorts, whereas strand bias was clearly evident in expressed genes (**Fig. 3e** and **3f**). The same trend could be observed in four independent breast cancer cohorts (PCAWG, Hartwig, POG570 and BRCA-EU) and liver cancer using tissue-specific replication orientations (**Fig. 3e** and **3f**). The expression-dependent strand bias was also evident in two independent ovarian cancer cohorts (**Supplementary Fig. S8a**). It is possible that gene expression is the consequence of SVs rather than the cause. We therefore used gene expression from normal tissues and still observed the expression-dependent replicated-strand bias in TD3 and TD4 (**Supplementary Fig. S8b** and **S8c**).

Taken together, we observe robust transcription-dependent replicated-strand bias in large TDs across multiple independent cancer cohorts.

Replicated-strand bias as an independent effect in large TDs

Next, we sought to assess the effect of replication in strand bias of large TDs. There are two types of TRCs: head-on (transcription and replication in the opposite orientations, **Fig. 1a**) and co-directional (transcription and replication in the same orientations) collisions. If large TDs result from TRCs, we expect the replicated-strand bias to be observed in both types of collisions. Indeed, in PCAWG and Hartwig cohorts, TD3 and TD4 displayed replicated-strand bias in both head-on and co-directional collisions (**Fig. 4a** and **4b**). The same was observed in BRCA-EU and Hartwig breast cancer cohorts when replication orientations were annotated from MCF7 cells (**Fig. 4a** and **4b**). These results suggest that the replicated-strand bias in large TDs depends on replication but not on the type (i.e., head-on vs co-directional) of collision.

Many genomic features, such as GC content, transcription, replication and chromatin state, are highly correlated. To rule out the possibility that replicated-strand bias in large TDs was due to other factors, we performed multivariate regression using SV strands (replicated or unreplicated) as the dependent variable and observed-VS-random SVs as well as a comprehensive list of

genomic features as dependent variables. We found observed SVs were significantly associated with replicated strands only in TD3 and TD4 when other genomic features were controlled for (**Supplementary Fig. S9a**) in the PCAWG cohort. The same significant associations were also observed in the Hartwig cohort (**Supplementary Fig. S9b**) as well as the four breast cancer cohorts combined using replication timing from MCF7 (**Supplementary Fig. S9c**). Therefore, the replicated-strand bias in large TDs was an independent effect that could not be explained by other genomic features.

Genetic and clinical associations of large TDs

We then sought to identify genes involved in TRC and large TD formation. We tested somatic SNVs in all protein-coding genes that altered coding sequences (**Supplementary Table S2**). As expected, *TP53* mutations were positively associated with large TDs (**Fig. 4c**) since they allow the cells to tolerate genome instability. *SPOP* mutations were also associated with large TDs in prostate cancer. Our recent finding that mutant SPOP is associated with complex SVs [32] suggests that mutant SPOP likely has a similar gatekeeper effect as mutant TP53. As we and others have previously reported [40–43], *CDK12* mutations, but not *BRCA1* or *BRCA2* mutations, are associated with large TDs in ovarian cancer and metastatic prostate cancer (**Fig. 4d** and **Supplementary Table S2**). *BRCA1* mutations are only associated with small TDs [4,44] but not large TDs. We focus on *CDK12* in greater detail in a later section. Interestingly, we found *PIK3CA* mutations were negatively associated with large TDs in four independent breast cancer cohorts (**Fig. 4e**). There are two possible reasons for somatic alterations to be mutually exclusive: the genes affect the same molecular pathway, or the alterations are incompatible (synthetic lethal). Although certain genes are recurrently altered by large TDs, large TDs affect many genes throughout tumor genomes. So, it is unlikely that large TDs always impact the same pathways as mutant PIK3CA. It is more likely that breast cancer cells with *PIK3CA* mutations cannot tolerate elevated TRCs. Moreover, *ARID1A* and *PTEN* mutations were negatively associated with large TDs in both primary and metastatic uterine cancers (**Fig. 4f**).

As mentioned above, large TDs recurrently amplify genes. In addition to genes previously reported, such as *MYC*, *MALAT1*, *MECOM*, *ESR1*, *ERBB2*, *FOXA1* and *MDM2* [37,45], we found *GATA3* was frequently amplified in metastatic breast cancer, and *ERBB3* and *H3F3B* were frequently amplified in uterine cancer (**Supplementary Fig. S10**).

Next, we tested whether large TDs could be used for prognosis. Abundant large TDs in tumors were associated with poor patient overall survival when all tumor types were combined in the PCAWG cohort as well as when patients were stratified by tumor *TP53* mutation status (**Fig. 4g**). Abundant large TDs were also associated with poor survival in two prostate cancer cohorts (PCAWG and PRAD-UK) as well as melanoma and esophageal cancer (**Fig. 4g**).

Loss of CDK12 leads to increased R-loops and TRCs

We have shown that *CDK12* mutations are associated with large TDs in cancer and that large TDs displayed footprints of TRCs. Therefore, we hypothesized that *CDK12* inactivation causes elevated TRCs. To test this hypothesis, we generated single-cell derived *CDK12* knockout (KO) clones using CRISPR/Cas9 in 22Rv1 prostate cancer cells. These KO clones were confirmed to lack CDK12 expression by western blotting (**Fig. 5a**). In addition, we validated the knockouts by whole-exome sequencing (WES) to demonstrate that we had successfully generated indels in exon 1 of *CDK12*, leading to frameshifts and early truncations in both alleles. This recapitulates the frameshift mutations found in castration-resistant prostate cancer (CRPC) patients (**Supplementary Fig. S11a** and **S11b**).

Because CDK12 controls transcription through phosphorylation of RNA polymerase II (RNAPII) [46,47] and regulates its processivity [48], we asked whether loss of CDK12 induces global changes in RNA-DNA hybrids, or R-loops. R-loops have previously been shown to be important regulators of genomic instability, particularly during DNA replication and DSB repair. Increased R-loops can impede efficient transcription and replication [49–51]. Interestingly, we found that in two independent *CDK12* KO clones, loss of CDK12 significantly increased total R-loops by approximately four-folds (**Fig. 5b** and **5c**). We next asked whether loss of CDK12 leads to increased TRCs, a potential consequence of increased R-loops that act as barriers to replication [52]. To evaluate this, we performed a proximity ligation assay (PLA) to measure the colocalization of RNA polymerase II and the DNA replication protein, PCNA. We found that *CDK12* KO cells had significantly increased PLA signals, indicative of elevated TRCs (**Fig. 5d** and **5e**). To test this using another silencing system, we generated *CDK12* knockdown cells using CRISPR interference (CRISPRi) [53] and found similar increases in TRCs (**Supplementary Fig. S11c** and **S11d**). We also assessed TRCs using *CDK12* KO cells in an independent prostate cancer cell line C42B and found similar observations (**Supplementary Fig. S11e** and **S11f**). The changes in R-loops and PLA were rescued by re-expressing wildtype CDK12 in the *CDK12* KO cells (**Fig. 5f**, **5g** and **5h**). Taken together, these results demonstrate that loss of CDK12 induces R-loops and TRCs in prostate cancer cells, which is consistent with our observations that CDK12-deficiency-related large TDs display unique genetic footprints of TRCs.

We propose the following working model to explain these observations (**Fig. 6a**). Dysregulation of RNA polymerase II and transcription due to loss of CDK12 leads to the formation of R-loops, which subsequently blocks PCNA and the replication fork. Ultimately, replication forks collapse. A previous study showed that stalled replication forks lead to small TDs in mutant BRCA1 background via three possible mechanisms—breakage fusion, microhomology-mediated break-induced repair (MMBIR), or replication restart-bypass [44]. The partner sister strand is rearranged in the breakage-fusion mechanism, whereas it is unrearranged in the latter two mechanisms. In cancer, large TDs do not co-occur with large deletions at the same loci, suggesting that large TDs likely form through either MMBIR or replication restart-bypass (**Fig. 6a**). Further study is required to elucidate the subsequent repair steps after the collision.

Large TDs as a biomarker for drug sensitivity

We sought to assess if large TDs and TRCs could induce drug sensitivities. We used the 325 cell lines in the Cancer Cell Line Encyclopedia (CCLE) that have WGS data, allowing us to accurately quantify large TDs. Among these cell lines, large-scale drug screening [54] has been conducted in 203 cell lines. We focused on drugs related to DNA damage, damage repair, DNA replication and transcription (**Supplementary Table S3**), and found that cancer cell lines with abundant large TDs were significantly more sensitive to two reagents that inhibit DNA repair—the WEE1 inhibitor MK-1775 (also known as AZD-1775) and the PARP inhibitor PJ-34 (**Fig. 6b**). WEE1 is a nuclear kinase regulating G2/M checkpoint transition and allows DNA repair before mitotic entry [55]. MK-1775 has shown potent activities when combined with DNA damaging agents [56]. We found that in the 22Rv1 prostate cancer cells, loss of CDK12 increased drug sensitivity to MK-1775 (**Fig. 6c** and **6d**). In addition, we found a similar increase in MK-1775 sensitivity in *CDK12* KO C42B prostate cancer cells (**Supplementary Fig. S12a** and **12b**). Although phase II clinical trials of MK-1775 have been conducted in ovarian, breast, lung, gastric cancers, etc. [57], our results suggest that patients of other tumor types, such as prostate, esophageal cancers, and even a small subset of liver cancers with high frequencies of large TDs (**Fig. 2d** and **2e**), may benefit from WEE1 inhibition. Furthermore, we found that cancer cell lines abundant in large TDs were resistant to three DNA synthesis inhibitors—bendamustine (DNA alkylating agent), nelarabine (guanine analog) and famciclovir (another guanine analog) (**Fig. 6b**). It is possible that cancer cells with abundant large TDs are already impaired in DNA synthesis due to frequent TRCs, or they have a mechanism in place to overcome replication roadblocks. Therefore, blocking DNA synthesis in these cells does not provide any additional benefit. Taken together, our results demonstrate that repurposing existing drugs, particularly those targeting DNA repair, may be a therapeutic strategy in tumors deficient in CDK12 and other cancers characterized by large TDs.

Discussion

Here, we report that large TDs in tumors result from accumulation and improper repair of TRCs. We first deconvoluted highly conserved somatic simple SV signatures from three independent pan-cancer WGS cohorts (the PCAWG, Hartwig and POG570). We reasoned that SVs formed via TRC would display replicated-strand bias. Indeed, we observed such bias in two large TD signatures. The replicated-strand bias in large TDs depended on transcription, could not be explained by any other genomic factors, and was reproducible in two pan-cancer cohorts as well as several other independent cohorts. Furthermore, we observed that *CDK12* mutations were associated with abundant large TDs in prostate and ovarian cancers. Experimentally, we demonstrated that knocking out or suppressing CDK12, a key regulator of mRNA transcription [58], led to increased TRCs and R-loops.

Large TDs are abundant in several tumor types, such as uterine, breast, ovarian, prostate, esophageal, stomach, and head and neck cancers **(Fig. 2d** and **2e**). Most tumors with abundant large TDs are female cancers and upper gastrointestinal tract cancers, which suggests that the tissues of origin may play a role. Oncogene activation is known to cause replication stress [12–17]. However, we did not observe activating mutations in oncogenes, such as *BRAF*, *KRAS*, *EGFR*, and *PIK3CA*, to be positively associated with large TDs in any cohorts. Instead, *PIK3CA* mutations were negatively associated with large TDs in four independent breast cancer cohorts (**Fig. 4e**). These results suggest that large TDs may not arise directly from oncogene-induced replication stress.

There remain multiple open questions, such as how loss of CDK12 leads to persistent R-loops and TRCs and how large TDs form after TRCs. Although previous work showed that co-directional collision reduces R-loop formation [18], we found no significant differences in large TDs between head-on and co-direction collisions except in the PCAWG cohort (**Fig. 4a** and **4b**). This suggests that the role of R-loops in the case of co-directional collisions in large TDs remains to be elucidated. Further mechanistic studies are required to fully understand the formation of R-loops and TRCs. Nonetheless, our data suggest that both R-loops and TRCs occur in the absence of CDK12. Once TRCs occur, replication forks stall and collapse, and the chromosomal breaks generate DNA DSBs. The DNA damage repair (DDR) system certainly plays an important role, likely recognizing replication fork blockage, DSBs, and stretches of ssDNA and activating cell cycle checkpoints mediated by ATM and ATR [59]. In addition, BRCA1 and BRCA2 have been shown to play roles in resolving R-loops [60–62]. In the context of CDK12 deficiency, prior studies have shown CDK12 controls the expression of many DNA repair genes, including BRCA1 and ATM, by regulating intronic polyadenylation [63–65]. This global DDR deficiency may lead to aberrant repair of TRCs, stalled replication forks undergoing break-induced repair or replication restart, and duplicated stretches of the genome. Therefore, it is also possible that loss of CDK12 does not directly promote the formation of TRCs, but instead, leads to TRC repair deficiency which subsequently causes the accumulation of TRCs in CDK12 deficient cells. Finally, our finding that numerous well-known oncogenes are found in large TD hotspots suggests that transcriptionally active pro-tumorigenic genes within the TDs are under positive selection during tumorigenesis.

Selectively targeting cancers harboring large TDs would be of considerable potential therapeutic utility. Prior studies suggested that large TDs may be a source of neoepitopes resulting from gene fusions, which can be recognized by the immune system [41]. A phase II clinical trial evaluating checkpoint immunotherapy in prostate and other cancers with *CDK12* mutations is currently underway [66]. Given the possible deficiencies in TRC repair and DNA replication in tumors with large TDs, we sought to uncover synthetic lethal vulnerabilities caused by CDK12 loss. Our data demonstrate that WEE1 may be an important therapeutic target in this context. Previous data showed that *TP53* mutation was not a reliable biomarker for WEE1 inhibitor efficacy [57]. Hence, large TDs and CDK12 mutations may be better biomarkers of MK-1775 sensitivity. Future studies will be needed to evaluate the efficacy of WEE1 inhibitor monotherapy and potential combinations for patients with these poor prognostic cancers harboring large TDs.

In summary, our study highlights the role of TRCs in large TD formation and suggests that large TDs may be a biomarker of response to WEE1 inhibition, revealing additional therapeutic strategies.

Data availability

The patient cohorts used in this study are summarized in **Supplementary Table S1**. There were 2,583 primary tumors in the PCAWG cohort [33], 2,367 metastatic tumors in the Hartwig Medical Foundation cohort [34], 570 metastatic tumors in the POG570 cohort [35], 532 primary breast cancers (BRCA-EU), 115 primary ovarian cancers (OV-AU) and 218 primary prostate cancers (PRAD-UK). Somatic variants (SNVs, CNVs and SVs), gene expression quantifications and clinical information (tumor histology and patient survival) were obtained from https://dcc.icgc.org/pcawg for PCAWG cohort, https://hartwigmedical.github.io for Hartwig cohort, https://www.bcgsc.ca/downloads/POG570/ for POG570 cohort, https://dcc.icgc.org/ for OV-AU and PRAD-UK cohorts. Gene expression data of BRCA-EU were provided by Dr. Marcel Smid. A subset of breast cancers in the PCAWG cohort had molecular subtypes annotated in a previous study [67]. Gene expression quantifications from tumor adjacent normal samples of the Cancer Genome Atlas (TCGA) cohort were downloaded from Genomic Data Commons (https://portal.gdc.cancer.gov/). Somatic SVs (CCLE2019 release) in 328 cancer cell lines and drug response data (PRISM Repurposing 19Q4) [54] were downloaded from the Cancer Dependency Portal (https://depmap.org/portal/download/all/). Human reference genome assembly GRCh37 (hg19) was used in the entire study. Reference genome mappability was obtained from https://bismap.hoffmanlab.org/.

Oncogenes were obtained from the COSMIC cancer gene census (https://cancer.sanger.ac.uk/census). GC content was calculated using bedtools for 50bp windows flanking both sides of each SV breakpoint. CpG islands, centromere, telomere, repeat annotation, and Lamina associated domains (LAD) for human Tig3 lung fibroblasts were downloaded from UCSC Genome Table Browser (https://genome.ucsc.edu/). Non-B DNA annotation was downloaded from non-B DB [68] (https://nonb-abcc.ncifcrf.gov/). ENCODE Chromatin Immunoprecipitation Sequencing (ChIP-Seq) data for H3k27ac, H3k27me3, H3k36me3, H3k4me1, H3k4me2, H3k4me3, H3k79me2, H3k9ac, H3k9me3, H4k20me1 of GM12878 cell line were downloaded from the UCSC composite track (http://genome.ucsc.edu/cgi-bin/hgFileUi?db=hg19&g=wgEncodeUwHistone). Nucleosome occupancy for the K562 cell line was downloaded from ENCODE (https://www.encodeproject.org/files/ENCFF000VNN/). Topologically associating domain (TAD) boundaries of GM12878 [69] were downloaded from NCBI (https://www.ncbi.nlm.nih.gov/geo/query/acc.cgi?acc=GSE63525).

WES data for CDK12 KO clones are deposited in National Institutes of Health (NIH) Sequence Read Archive (SRA) under BioProject ID PRJNA932332.

All data described above are publicly available.

Code availability

Custom scripts used in this study can be found at:

https://github.com/yanglab-computationalgenomics/TRC.SV.strand.bias

Methods

Simple SVs and simple SV signatures

Clustered complex SVs detected by Starfish and non-clustered complex SVs, such as chromoplexy and cycles of insertions, detected by junction patterns [2] were removed from raw somatic SVs. The remainder of SVs were simple SVs and classified into nine types—deletions, fragile site deletions, TDs, fragile site TDs, foldback inversions (breakpoints within 50kb in distance), unbalanced inversion, reciprocal inversions, unbalanced translocations and reciprocal translocations (**Supplementary Fig. S2**). Fragile sites annotation was obtained from the PCAWG SV study [2]. Deletions, TDs and inversions were further divided by size (**Fig. 1b**). As a result, a total of 49 simple SV classes were defined (**Fig. 1b**). Simple SV signatures were extracted using SigProfilerExtractor [36] with default parameters in PCAWG, Hartwig and POG570 cohorts. In PCAWG cohort, deletions ranging in size 0-5kb, 5kb-25kb, 25kb-500kb, 500kb-5Mb were assigned to signatures "Del1", "Del2", "Del3", and "Del4", while TDs ranging in 0-10kb, 10kb-100kb, 100kb-500kb, 500kb-7.5Mb were assigned to signatures "TD1", "TD2", "TD3", and "TD4". Deletions greater than 5Mb, TDs greater than 7.5Mb, reciprocal inversions, and reciprocal translocations were assigned to signature "Large mixed". In the Hartwig cohort, deletions ranging in size 0-1kb, 1kb-5kb, 5kb-25kb, 25kb-500kb, and 500kb-5Mb were assigned to signatures "Del0" to "Del4", TDs ranging in 0-1kb, 2kb-10kb, 10kb-100kb, 100kb-750kb, and 750kb-7.5Mb were assigned to signatures "TD0" to "TD4". Foldback inversions and unbalanced inversions less than 5Mb were assigned to signature "Fb inv". Deletions greater than 5Mb, TDs greater than 7.5Mb, unbalanced inversions greater than 5Mb, reciprocal inversions, and reciprocal translocations were designated to signature "Large mixed".

Replication orientation annotation

The raw replication timing data for fourteen cell lines derived from solid tissues (A13, BG01 NPC, BG02 ESC, CyT49_Definitive_Endoderm, CyT49_Liver, CyT49_Neural_Crest, CyT49_Panc, HCT116, HEK293, HeLaS3, HepG2, MCF7, RPE1 hTERT, and U2OS) were downloaded from https://www2.replicationdomain.com. The replication timing data were quantile normalized across all cell lines. The reference genome was divided into bins of 50kb in size and the normalized values were averaged within the bins. The replication timing slope was calculated for adjacent bins, and then the replication orientations, "left-replicated" and "right-replicated", were determined for sharp transition bins (slope < 5e-7) but not for flat regions (**Supplementary Fig. S6**). The replication orientations of protein-coding genes were assigned accordingly if the genes were entirely located in either left-replicated or right-replicated regions. There were between 6,581 to 9,548 genes annotated as left- and right-replicated per cell line. If the replication orientations of a gene were the same in 8 out of 14 cell lines, the gene was considered to have conserved replication orientation. There were 3,493 genes with conserved replication orientations in solid tissues. Protein-coding genes with the opposite transcription and DNA replication orientations would have head-on collisions whereas the ones with the same transcription and DNA replication orientations would have co-directional collisions.

Strand bias test

For each somatic SV observed in tumors, two random SVs were generated by placing the same SV to random uniquely mappable locations of the same chromosome with SV type and size preserved. SV breakpoint orientations were assigned as in **Supplementary Fig. S5.** Deletions and TDs entirely residing within protein-coding genes (both breakpoints located in the same genes) were discarded because deletions and TDs have both "+" and "-" breakpoints (**Supplementary Fig. S5**). We reasoned that even if they truly resulted from transcription and replication collision, the strand effect would be cancelled out by the mixture of "+" and "-" breakpoints in these SVs. The breakpoints of the remainder of SVs were considered individually. Only the breakpoints located in non-overlapping protein-coding genes with defined replication orientations were used to test for strand bias. SV breakpoints located in overlapping protein-coding genes were discarded because these gene often had different expression levels. Breakpoints in intergenic regions or in genes without defined replication orientations were also discarded. Then, each SV breakpoint in protein-coding genes was assigned as "replicated" or "unreplicated" based on the breakpoint orientation and replication orientation. For each SV signature, a two-by-two table ("replicated/unreplicated" and "observed/random SVs") was constructed and replicated-strand bias in observed SVs was tested by two-sided Fisher's exact test followed by Bonferroni correction. Corrected *P* values that were less than 0.05 were considered significant. All protein-coding genes were ranked based on the expression levels (upper-quartile normalized FPKM or adjusted TPM) in each tumor sample when RNAseq data were available, and the top 75% genes were defined as "expressed" whereas the bottom 25% were "unexpressed". When defining "expressed" and "unexpressed" genes by gene expression in normal samples, genes were ranked by median expression levels of adjacent normal samples in tumor types from TCGA of which RNAseq data were available for at least 20 normal samples.

Logistic regression was performed to take other genomic features into account in addition to gene expression and replication timing. The genomic features included GC content, CpG island, SV breakpoint distance to centromere, breakpoint distance to telomere, breakpoint distance to various repetitive elements (Alu, L1, L2, LTR, MIR elements, DNA transposons and low complexity repeats), breakpoint distance to non-B DNA motifs, histone markers, nucleosome occupancy, LAD, and breakpoint distance to TAD boundaries. All distances were log10 transformed. Signal enrichment values (density of modifications in 25bp window) of histone modifications at the SV breakpoints were used. The proportion of bases in LAD at a 1Mb window flanking breakpoints were calculated. The dependent variable was replicated/unreplicated strand of SV breakpoints. The above features, along with observed/random SV, gene expression, replication timing, and the interaction of gene expression and replication timing, were independent variables.

Genetic and clinical associations of large TDs

Somatic SVs in TD3 and TD4 in both PCAWG and Hartwig cohorts were defined as large TDs (TDs with sizes ranging between 100kb and 7.5Mb not in fragile sites). Linear regression was performed to test the associations between frequencies of large TDs and genes with protein-coding altering SNVs. Mutation load was included as a covariate in all regression models and tumor type was modelled as a covariate in the pan-cancer analysis. Large TD frequency and mutation load were log10 transformed. Only protein-coding genes with mutation frequencies of at least 3% at pan-cancer level and at least 4% in individual tumor types were considered. FDR was calculated by Benjamini-Hochberg procedure and 0.1 was used as the significance cutoff. A 10% mutation frequency cutoff was used for uterus cancers in the Hartwig cohort due to their high mutation load. GISTIC2 [70] was used to identify genomic regions with recurrent large TDs. The confidence level was set at 0.9 and default values were used for all other parameters. Log rank test was performed for survival analysis. Patients with at least 10 large TDs in their tumors were compared to those without any large TDs stratified by *TP53* mutation status and tumor type.

In silico drug sensitivity test

Complex SVs in CCLE cell lines were removed as previously described. Three cell lines, LK2_LUNG, SNU16_STOMACH, and NCIH1436_LUNG, were discarded due to the presence of too many likely artifactual small TDs. Only drug dose response scores from the HTS002 screen were used [54] since it was the largest screen (1,394 drugs, 480 cell lines and 592,912 drug x cell line combinations). Drugs in the following categories were tested—DNA damage agents, DNA damage repair inhibitors, DNA replication inhibitors and transcription inhibitors (**Supplementary Table S3**). For each drug, Kendall's Tau correlation coefficient was calculated between large TD frequencies and area under the ROC Curve of the drug in all cell lines.

Cell culture

22Rv1 cells were obtained from the American Type Culture Collection (ATCC) and C42B cells were obtained from the University of Michigan. Cells were grown in standard conditions with antibiotics (RPMI-1640 with 10% FBS) and routinely tested for mycoplasma (Lonza). Cell lines were all validated by STR DNA profiling (Genetica). Cells were transduced with NucLightRed (Sartorius) according to the manufacturer’s instructions.

Plasmids and cloning

pSpCas9(BB)-2A-GFP (PX458) (Addgene plasmid # 48138) was obtained from Dr. Feng Zhang. pDONR221 was from Thermo Fisher Scientific. Full-length CDK12 cDNA was a gift from Dr. Gregg Morin and Dr. Grace Cheng as previously described [71]. Cloning was performed using standard protocols. For CRISPR interference (CRISPRi) assays, cells were transduced with dCas9 from pHR-SFFV-dCas9-BFP-KRAB (Addgene plasmid 46911) and sgRNA sequences

were cloned into pCRISPRia-v2 (Addgene plasmid #84832), both from Dr. Jonathan Weissman. For Gateway cloning, BP and LR Clonase II (Thermo Fisher Scientific) reactions were performed according to the manufacturer's protocol. Gel purification was performed using the NucleoSpin Gel and PCR Clean-up kit (Takara Bio Inc.) according to the manufacturer's protocol. Annealed sgRNAs were ligated into the plasmid using the Quick Ligation Kit (New England BioLabs) according to the manufacturer's protocol.

Lentiviral production

Lentiviral production was carried out using calcium-phosphate-mediated transfection of HEK293T-Lenti-X cells using standard procedures. Lentivirus was concentrated using the Lenti-X concentrator (Takara Bio Inc.) according to the manufacturer's protocol. Stably transduced cells were selected with blasticidin (3 µg/ml, Gibco) or puromycin (3 µg/ml, Gibco) for at least 5 days.

Generation of CDK12 knockout and knockdown cells

22RV1 or C42B cells were transfected with the PX458 plasmid containing the CRISPR/Cas9 and the guide targeting CDK12 using Lipofectamine 3000 (Thermo Fisher) according to manufacturer's instructions. 48-72 hours after transfection, cells were sorted for green fluorescence protein (GFP) expression, and then into single cells in a 96-well plate format using a FACS Aria. Guide sequences to knockout CDK12 were sg1: 5' GCTTGTGCTTCGATACCAA 3' and sg2: 5' ACTTTGCAGCCGTCATCGGG. Clones were expanded and validated by Western blotting and by sequencing the target site. To knockdown CDK12 using CRISPR interference (CRISPRi) the following guide was used: 5' GTGAGAAGCCGACGGCCCG 3' (CDK12sg).

Western blotting

Cells were lysed in RIPA buffer the Halt protease and a phosphatase inhibitor cocktail (Thermo Fisher Scientific). Protein concentration was measured using the BCA Protein Assay Kit (Thermo Scientific). Lysates were mixed at a 1:1 ratio with Laemmli Buffer (Bio-Rad) supplemented with beta-mercaptoethanol, boiled at 95°C, and then subjected to SDS-PAGE, transferred to PVDF membranes, blocked in 5% w/v BSA, incubated with primary antibody overnight. The next day, Horseradish Peroxidase (HRP) conjugated secondary antibodies (Cell Signaling, 1:8000) were used and the blot was visualized using ECL Detection Reagents (Genesee Scientific). Antibodies used included: CDK12 (Atlas #HPA008038, 1:1000), GAPDH (Cell Signaling, 1:2000) and Lamin B1 (Cell Signaling, 1:1000).

S9.6 slot blotting

Total genomic nucleic acids were purified by lysing cells with standard Proteinase K/SDS/Tris-EDTA lysis buffer followed by standard phenol/chloroform/isoamyl alcohol pH 8.0 extraction and ethanol precipitation. Samples were digested overnight using a restriction enzyme cocktail of BsrgI, EcoRI, HindIII, SspI, and XbaI in Buffer r2.1 (NEB), followed by a 30-minute incubation with RNase A (Thermo Scientific) in 500mM NaCl to remove free RNA. Genomic DNA was extracted as before and precipitated in isopropanol/NaOAc. As a negative control, 8 μg of each sample was treated with RNase H (NEB) at 37°C overnight and then purified as before. 500ng of each sample was spotted onto two wells of positively charged Nylon membrane (Roche) using a slot blot apparatus (BioRad) and vacuum suction. As a separate loading control, half of the membrane was denatured in 0.5M NaOH, 1.5M NaCl, then neutralized for 10 minutes in 1M NaCl, 0.5M Tris-HCl pH 7.0. Membranes were UV crosslinked (0.12J/m^2) and then blocked in 5% milk/TBST. Membranes were then incubated overnight with either S9.6 (Kerafast) or ssDNA (Millipore) antibodies, then washed and incubated with anti-mouse secondary-HRP antibodies (Cell Signaling) for 1 hour at RT before exposure to ECL.

Detection of transcription-replication collisions

The proximity ligation assay (PLA) was carried out as previously described [72]. Briefly, cells were seeded at 50,000 cells/well in Ibidi u-Slide 8-well slides (#80806) pre-coated with poly-lysine. Cells were allowed to adhere overnight. The next day, DRB (5,6-Dichlorobenzimidazole 1-β-D-ribofuranoside) was added to wells as a negative control and incubated for 4 hours. Then, cells were washed twice with PBS and then treated with CSK extraction buffer (0.2% Triton X-100, 20 mmol/L HEPES-KOH pH 7.9, 100 mmol/L NaCl, 3 mmol/L $MgCl_2$, 300 mmol/L sucrose, 1 mmol/L EGTA) on ice for 3 minutes. Cells were fixed on ice with 4% paraformaldehyde, then ice-cold methanol, and then permeabilized in PBS/0.5% Triton X-100 (PBST) and blocked with 3% BSA in PBST for 1 hour. Afterwards, cells were incubated with the indicated primary antibodies (PCNA, Santa Cruz, 1:500; p-RNAPII Ser2, Novus, 1:1000) overnight at 4°C. The next day, cells were incubated with anti-mouse minus and anti-rabbit plus PLA probes (Sigma, DUO92002 and DUO92004) at 37°C for 1 hour. The PLA reaction was performed using Duolink In Situ Detection Red (Sigma, DUO92008), according to the manufacturer's instructions. Cells were stained with DAPI after completing the washing steps. Images were captured with a Nikon 90i confocal microscope and the PLA signal was quantified using CellProfiler as previously described. Statistical testing was performed using Prism software (GraphPad 9) and $P<0.05$ was considered statistically significant after correcting for multiple comparisons using either ANOVA or Kruskal-Wallis test as described in the figure caption.

Drug dose-response assays

Cells were seeded in a 96-well plate at a density of 1,000 cells per well overnight. The next day, either MK-1775 (MedChemExpress) or DMSO was added. Cells were exposed to the drug for 15-25 days, and cell confluency or nuclei count was measured using an IncuCyte S3 (Sartorius).

577

Acknowledgements

We thank the Center for Research Informatics at the University of Chicago for providing the computing infrastructure. We thank Jace Chen for assistance in artwork, Dr. Kari Herrington for microscopy assistance, and the Nikon Imaging Center at UCSF. The work was supported by the University of Chicago and UChicago Comprehensive Cancer Center (L.Y.). The work was also supported by Young Investigator Awards from the Prostate Cancer Foundation (to J.C. and H.L.), a Challenge Award from the Prostate Cancer Foundation (to F.Y.F.), the Department of Defense Physician's Research Award (W81XWH-20-1-0136 to J.C.), as well as funds from the Benioff Initiative for Prostate Cancer Research at UCSF (to J.C., M.K., F.Y.F. and A.A.) and the Martha and Bruce Atwater Breast Cancer Research Program at UCSF (to M.K.).

Disclosure

A. Ashworth reports personal fees from Tango Therapeutics, Azkarra Therapeutics, Ovibio, Kytarro, Cytomx, Cambridge Science Corporation, Genentech, Gladiator, Circle, Bluestar, Earli, Ambagon, Trial Library, Phoenix Molecular Designs, GSK, Prolynx; grants from SPARC, and AstraZeneca outside the submitted work; in addition, he holds patents on the use of PARP inhibitors held jointly with AstraZeneca from which he has benefited financially (and may do so in the future).

F.Y. Feng reports personal fees from Bluestar Genomics, Astellas, Foundation Medicine, Exact Sciences, Tempus, POINT Biopharma, Janssen, Bayer, Myovant, Roivant, SerImmune, Bristol Meyers Squibb, Novartis, and personal fees from POINT Biopharma outside the submitted work and other support from Artera.

J. Chou reports consulting fees from Exai Bio outside the submitted work.

Figure Legends

Figure 1. Transcription-replication collision and simple SV signatures. a, Diagram of the transcription and DNA replication collision producing SVs. The dark and light blue arrows in the left panel represent leading and lagging strands, respectively. The right panel illustrates an SV resulting from the collision. One of the replicated strands after the collision is ligated with a partner DNA fragment. The resulting SV can be either intra-chromosomal or inter-chromosomal, depending on the source of the SV partner. **b** and **c**, Simple SV signatures of 2,583 primary tumors in the PCAWG cohort and 2,367 metastatic tumors in the Hartwig cohort. Simple SVs are classified into four broad categories (Del, deletion; TD, tandem duplication; Inv, inversion; and Tra, translocation) and further into 49 categories based on size. The names of signatures are listed at the top. The lengths of the bars indicate the relative contributions of different categories to the corresponding signatures.

Figure 2. Pan-cancer replicated-strand bias and large TD frequencies across tumor types. a, An example of normalized replication timing of MCF7 cell line. The blue and green curves represent right- and left-replicated regions (sharp transition regions). **b** and **c**, Replicated-strand bias for primary tumors in the PCAWG cohort and metastatic tumors in the Hartwig cohort. Each signature and its number of observed breakpoints are shown on the y-axis. *P* values are calculated by Fisher's exact test. The x-axis shows Bonferroni-adjusted *P* values. The dashed black line on the x-axis represents a 0.05 adjusted *P* value cutoff. Conserved replication orientation is used for both cohorts. **d** and **e**, The numbers of large TDs in the PCAWG and Hartwig cohorts. Black dots represent individual tumors grouped by tumor type. Tumor types are annotated at the bottom of the plots. Two numbers after tumor type names are sample size and the proportion of samples with >= 10 large TDs in the corresponding tumor types. Tumor types with at least 20 tumors are shown and are sorted by the proportion of samples with >= 10 large TDs.

Figure 3. Tumor-type-specific and transcription-dependent replicated-strand bias. a, Replicated-strand bias in primary breast and liver cancers using replication orientations defined from the MCF7 and HepG2 cell lines. *P* values are calculated by Fisher's exact test. The x-axis shows Bonferroni-adjusted *P* values. **b**, Replicated-strand bias in metastatic breast cancers using replication orientations defined from the MCF7 cell line. **c**, Replicated-strand bias in primary ovarian and prostate cancers. **d**, Replicated-strand bias in metastatic ovarian, prostate, and esophageal cancers. **e** and **f**, Replicated-strand bias in unexpressed genes and expressed genes for primary and metastatic tumors. The tested tumor type, sample size and source of replication orientations are annotated at the top of each plot.

Figure 4. Replicated-strand bias in head-on and co-directional collision regions, and genetic and clinical associations of large TDs. a and **b**, Replicated-strand bias in head-on and co-directional collision regions in primary and metastatic cancers. The testing cohorts, tumor types, sample sizes, sources of replication orientation, head-on and co-directional collision regions are annotated on the top of the plots. *P* values are calculated by Fisher's exact test. The x-axis shows Bonferroni-adjusted *P* values. **c**, *TP53* mutations positively associated with large TDs in the PCAWG, Hartwig, and POG570 cohorts. The x-axis denotes individual tumors. The red bars

indicate tumors with protein-altering somatic mutations. Cohort names and sample sizes are annotated above the plots. *P* values are calculated by linear regression with mutation load as covariates. Benjamini-Hochberg procedure is used to derive false discovery rates (FDRs). **d**, *SPOP* and *CDK12* mutations positively associated with large TDs in the PCAWG prostate, Hartwig prostate and PCAWG ovarian cancers. **e**, *PIK3CA* mutations negatively associated with large TDs in four independent breast cancer cohorts. **f**, *ARID1A* and *PTEN* mutations negatively associated with large TDs in the PCAWG and Hartwig uterus cancers. **g**, Kaplan-Meier survival plots for patients with at least 10 large TDs and no large TD in their tumors. *P* values are calculated by log rank test. Cohorts and *TP53* mutation status are annotated on top of plots.

Figure 5. Loss of CDK12 resulting in increased R-loops and TRCs. a, Western blot (WB) showing CDK12 in 22Rv1 control (Ctrl) and two *CDK12* KO clones (KO1 and KO2). GAPDH is shown as the loading control. **b**, Slot blot in 22Rv1 and *CDK12* KO cells showing S9.6 (R-loops). RNAse H1 addition is used as a control. Single strand (ss) DNA blot is shown as the loading control. **c**, Quantification of relative S9.6/ssDNA signal (n=8 independent experiments). **d**, Examples of confocal microscopy images in 22Rv1 Ctrl and *CDK12* KO cells. Blue indicates nuclei (DAPI) and red indicates PLA signal. DRB is used as a negative control. **e**, Quantification of the mean PLA signal per image per nuclei in 22Rv1 Ctrl and CDK12 KO cells (n=30 fields in one representative experiment). Three independent experiments were performed. **f**, WB showing CDK12 in 22Rv1 Ctrl, *CDK12* KO, and *CDK12* KO re-expressing wildtype CDK12. GAPDH is shown as the loading control. **g**, Quantification of S9.6 slot blot showing S9.6/ssDNA signal in *CDK12* KO re-expressing wildtype CDK12 cells (n=5 independent experiments). **h**, Quantification of the mean PLA signal per image per nuclei in *CDK12* KO + CDK12 re-expressing cells. In **c**, **e**, **g** and **h**, *P* values are calculated using ANOVA and corrected for multiple tests. Boxplots show medians (top bounds of boxes), standard errors of the mean (error bars) and individual data points (black dots, squares, triangles, and diamonds).

Figure 6. Drug sensitivity and final model. a, Working model of CDK12 loss leading to increased R-loops, TRCs and large TDs. **b**, Drug sensitivity measured by area under the curve (AUC) in association with the number of large TDs in cancer cell lines. Smaller values of AUC indicate cells are more sensitive to the drug, whereas large values indicate cells are more resistant. *P* values are calculated by Kendall test. **c** and **d**, Phase contrast images (**c**) and growth curves (**d**) of control (Ctrl) 22Rv1 and *CDK12* KO cells (KO1 and KO2) treated with DMSO or 1 μM of MK-1775 for 15 days. Phase contrast images shown with the confluency mask (orange) are from day 15. *P* values are calculated by Student's t test at day 15. Error bars represent standard errors of the mean.

References

1. Yang, L. *et al.* Diverse mechanisms of somatic structural variations in human cancer genomes. *Cell* **153**, 919–929 (2013).

2. Li, Y. *et al.* Patterns of somatic structural variation in human cancer genomes. *Nature* **578**, 112–121 (2020).

3. Lee, J.-K., Choi, Y.-L., Kwon, M. & Park, P. J. Mechanisms and Consequences of Cancer Genome Instability: Lessons from Genome Sequencing Studies. *Annu. Rev. Pathol. Mech. Dis.* **11**, 283–312 (2016).

4. Nik-Zainal, S. *et al.* Landscape of somatic mutations in 560 breast cancer whole-genome sequences. *Nature* **534**, 47–54 (2016).

5. Alt, F. W., Zhang, Y., Meng, F. L., Guo, C. & Schwer, B. Mechanisms of programmed DNA lesions and genomic instability in the immune system. *Cell* vol. 152 417–429 (2013).

6. Hakim, O. *et al.* DNA damage defines sites of recurrent chromosomal translocations in B lymphocytes. *Nature* **484**, 69–74 (2012).

7. Burke, W. *et al.* Recommendations for follow-up care of individuals with an inherited predisposition to cancer. II. BRCA1 and BRCA2. Cancer Genetics Studies Consortium. *JAMA* **277**, 997–1003 (1997).

8. Fong, P. C. *et al.* Inhibition of Poly(ADP-Ribose) Polymerase in Tumors from BRCA Mutation Carriers. *N. Engl. J. Med.* **361**, 123–134 (2009).

9. Farmer, H. *et al.* Targeting the DNA repair defect in BRCA mutant cells as a therapeutic strategy. *Nat. 2005 4347035* **434**, 917–921 (2005).

10. Gaillard, H., García-Muse, T. & Aguilera, A. Replication stress and cancer. *Nat. Rev. Cancer* **15**, 276–280 (2015).

11. Macheret, M. & Halazonetis, T. D. DNA replication stress as a hallmark of cancer. *Annu. Rev. Pathol. Mech. Dis.* **10**, 425–448 (2015).

12. Denko, N. C., Giaccia, A. J., Stringer, J. R. & Stambrook, P. J. The human Ha-ras oncogene induces genomic instability in murine fibroblasts within one cell cycle. *Proc. Natl. Acad. Sci. U. S. A.* **91**, 5124–5128 (1994).

13. Vafa, O. *et al.* c-Myc can induce DNA damage, increase reactive oxygen species, and mitigate p53 function: A mechanism for oncogene-induced genetic instability. *Mol. Cell* **9**, 1031–1044 (2002).

14. Bartkova, J. *et al.* Oncogene-induced senescence is part of the tumorigenesis barrier imposed by DNA damage checkpoints. *Nature* **444**, 633–637 (2006).

15. Di Micco, R. *et al.* Oncogene-induced senescence is a DNA damage response triggered by DNA hyper-replication. *Nature* **444**, 638–642 (2006).

16. Jones, R. M. *et al.* Increased replication initiation and conflicts with transcription underlie

Cyclin E-induced replication stress. *Oncogene* **32**, 3744–3753 (2013).

17. Macheret, M. & Halazonetis, T. D. Intragenic origins due to short G1 phases underlie oncogene-induced DNA replication stress. *Nature* **555**, 112–116 (2018).

18. Hamperl, S., Bocek, M. J., Saldivar, J. C., Swigut, T. & Cimprich, K. A. Transcription-Replication Conflict Orientation Modulates R-Loop Levels and Activates Distinct DNA Damage Responses. *Cell* **170**, 774-786.e19 (2017).

19. García-Muse, T. & Aguilera, A. Transcription-replication conflicts: How they occur and how they are resolved. *Nat. Rev. Mol. Cell Biol.* **17**, 553–563 (2016).

20. Helmrich, A., Ballarino, M. & Tora, L. Collisions between Replication and Transcription Complexes Cause Common Fragile Site Instability at the Longest Human Genes. *Mol. Cell* **44**, 966–977 (2011).

21. Sankar, T. S., Wastuwidyaningtyas, B. D., Dong, Y., Lewis, S. A. & Wang, J. D. The nature of mutations induced by replication-transcription collisions. *Nature* **535**, 178–181 (2016).

22. Seplyarskiy, V. B. *et al.* Population sequencing data reveal a compendium of mutational processes in the human germ line. *Science* **373**, 1030–1035 (2021).

23. Liang, K. *et al.* Targeting Processive Transcription Elongation via SEC Disruption for MYC-Induced Cancer Therapy. *Cell* **175**, 766-779.e17 (2018).

24. Laham-Karam, N., Pinto, G. P., Poso, A. & Kokkonen, P. Transcription and Translation Inhibitors in Cancer Treatment. *Frontiers in Chemistry* vol. 8 276 (2020).

25. Forment, J. V. & O'Connor, M. J. Targeting the replication stress response in cancer. *Pharmacology and Therapeutics* vol. 188 155–167 (2018).

26. Groelly, F. J., Fawkes, M., Dagg, R. A., Blackford, A. N. & Tarsounas, M. Targeting DNA damage response pathways in cancer. *Nat. Rev. Cancer 2022* 1–17 (2022) doi:10.1038/s41568-022-00535-5.

27. Alexandrov, L. B. *et al.* Signatures of mutational processes in human cancer. *Nature* **500**, 415–421 (2013).

28. Alexandrov, L. B. *et al.* The repertoire of mutational signatures in human cancer. *Nature* **578**, 94–101 (2020).

29. Macintyre, G. *et al.* Copy number signatures and mutational processes in ovarian carcinoma. *Nat. Genet.* **50**, 1262–1270 (2018).

30. Steele, C. D. *et al.* Signatures of copy number alterations in human cancer. *Nat. 2022 6067916* **606**, 984–991 (2022).

31. Drews, R. M. *et al.* A pan-cancer compendium of chromosomal instability. *Nat. 2022 6067916* **606**, 976–983 (2022).

32. Bao, L., Zhong, X., Yang, Y. & Yang, L. Starfish infers signatures of complex genomic rearrangements across human cancers. *Nat. Cancer 2022* 1–13 (2022)

doi:10.1038/s43018-022-00404-y.

33. Campbell, P. J. *et al.* Pan-cancer analysis of whole genomes. *Nature* **578**, 82–93 (2020).

34. Priestley, P. *et al.* Pan-cancer whole-genome analyses of metastatic solid tumours. *Nature* **575**, 210–216 (2019).

35. Pleasance, E. *et al.* Pan-cancer analysis of advanced patient tumors reveals interactions between therapy and genomic landscapes. *Nat. Cancer 2020 14* **1**, 452–468 (2020).

36. Islam, S. M. A. *et al.* Uncovering novel mutational signatures by de novo extraction with SigProfilerExtractor. *Cell Genomics* **0**, 100179 (2022).

37. Menghi, F. *et al.* The Tandem Duplicator Phenotype Is a Prevalent Genome-Wide Cancer Configuration Driven by Distinct Gene Mutations. *Cancer Cell* **34**, 197-210.e5 (2018).

38. Drier, Y. *et al.* Somatic rearrangements across cancer reveal classes of samples with distinct patterns of DNA breakage and rearrangement-induced hypermutability. *Genome Res.* **23**, 228–235 (2013).

39. Reusswig, K.-U. *et al.* Unscheduled DNA replication in G1 causes genome instability and damage signatures indicative of replication collisions. *Nat. Commun. 2022 131* **13**, 1–20 (2022).

40. Popova, T. *et al.* Ovarian cancers harboring inactivating mutations in CDK12 display a distinct genomic instability pattern characterized by large tandem duplications. *Cancer Res.* **76**, 1882–1891 (2016).

41. Wu, Y. M. *et al.* Inactivation of CDK12 Delineates a Distinct Immunogenic Class of Advanced Prostate Cancer. *Cell* **173**, 1770-1782.e14 (2018).

42. Viswanathan, S. R. *et al.* Structural Alterations Driving Castration-Resistant Prostate Cancer Revealed by Linked-Read Genome Sequencing. *Cell* **174**, 433–447 (2018).

43. Quigley, D. A. *et al.* Genomic Hallmarks and Structural Variation in Metastatic Prostate Cancer. *Cell* **174**, 758-769.e9 (2018).

44. Willis, N. A. *et al.* Mechanism of tandem duplication formation in BRCA1-mutant cells. *Nature* **551**, 590 (2017).

45. Fu, X. *et al.* FOXA1 upregulation promotes enhancer and transcriptional reprogramming in endocrine-resistant breast cancer. *Proc. Natl. Acad. Sci. U. S. A.* **116**, 26823–26834 (2019).

46. Bartkowiak, B. *et al.* CDK12 is a transcription elongation-associated CTD kinase, the metazoan ortholog of yeast Ctk1. *Genes Dev.* **24**, 2303–2316 (2010).

47. Tellier, M. *et al.* CDK12 globally stimulates RNA polymerase II transcription elongation and carboxyl-terminal domain phosphorylation. *Nucleic Acids Res.* **48**, 7712 (2020).

48. Chirackal Manavalan, A. P. *et al.* CDK12 controls G1/S progression by regulating RNAPII processivity at core DNA replication genes. *EMBO Rep.* **20**, (2019).

49. Crossley, M. P., Bocek, M. & Cimprich, K. A. R-Loops as Cellular Regulators and

Genomic Threats. *Mol. Cell* **73**, 398–411 (2019).

50. Brickner, J. R., Garzon, J. L. & Cimprich, K. A. Walking a tightrope: The complex balancing act of R-loops in genome stability. *Mol. Cell* **82**, 2267–2297 (2022).

51. Marnef, A. & Legube, G. R-loops as Janus-faced modulators of DNA repair. *Nat. Cell Biol.* **23**, 305–313 (2021).

52. Hamperl, S. & Cimprich, K. A. Conflict Resolution in the Genome: How Transcription and Replication Make It Work. *Cell* **167**, 1455–1467 (2016).

53. Gilbert, L. A. *et al.* CRISPR-mediated modular RNA-guided regulation of transcription in eukaryotes. *Cell* **154**, 442 (2013).

54. Corsello, S. M. *et al.* Discovering the anti-cancer potential of non-oncology drugs bysystematic viability profiling. *Nat. cancer* **1**, 235 (2020).

55. Matheson, C. J., Backos, D. S. & Reigan, P. Targeting WEE1 Kinase in Cancer. *Trends Pharmacol. Sci.* **37**, 872–881 (2016).

56. Hirai, H. *et al.* Small-molecule inhibition of Wee1 kinase by MK-1775 selectively sensitizes p53-deficient tumor cells to DNA-damaging agents. *Mol. Cancer Ther.* **8**, 2992–3000 (2009).

57. Kong, A. & Mehanna, H. WEE1 Inhibitor: Clinical Development. *Curr. Oncol. Rep.* **23**, (2021).

58. Chou, J., Quigley, D. A., Robinson, T. M., Feng, F. Y. & Ashworth, A. Transcription-Associated Cyclin-Dependent Kinases as Targets and Biomarkers for Cancer Therapy. *Cancer Discov.* **10**, 351–370 (2020).

59. García-Muse, T. & Aguilera, A. R Loops: From Physiological to Pathological Roles. *Cell* **179**, 604–618 (2019).

60. Bhatia, V. *et al.* BRCA2 prevents R-loop accumulation and associates with TREX-2 mRNA export factor PCID2. *Nature* **511**, 362–365 (2014).

61. Hill, S. J. *et al.* Systematic screening reveals a role for BRCA1 in the response to transcription-associated DNA damage. *Genes Dev.* **28**, 1957–1975 (2014).

62. Hatchi, E. *et al.* BRCA1 recruitment to transcriptional pause sites is required for R-loop-driven DNA damage repair. *Mol. Cell* **57**, 636–647 (2015).

63. Blazek, D. *et al.* The Cyclin K/Cdk12 complex maintains genomic stability via regulation of expression of DNA damage response genes. *Genes Dev.* **25**, 2158–2172 (2011).

64. Dubbury, S. J., Boutz, P. L. & Sharp, P. A. CDK12 regulates DNA repair genes by suppressing intronic polyadenylation. *Nature* vol. 564 141–145 (2018).

65. Krajewska, M. *et al.* CDK12 loss in cancer cells affects DNA damage response genes through premature cleavage and polyadenylation. *Nat. Commun. 2019 101* **10**, 1–16 (2019).

66. Alva, A. S. *et al.* Phase 2 trial of immunotherapy in tumors with CDK12 inactivation

(IMPACT): Results from cohort A of patients (pts) with metastatic castration resistant prostate cancer (mCRPC) receiving dual immune checkpoint inhibition (ICI). *https://doi.org/10.1200/JCO.2022.40.6_suppl.103* **40**, 103–103 (2022).

67. Ciriello, G. *et al*. Comprehensive Molecular Portraits of Invasive Lobular Breast Cancer. *Cell* **163**, 506–519 (2015).

68. Cer, R. Z. *et al.* Non-B DB v2.0: a database of predicted non-B DNA-forming motifs and its associated tools. *Nucleic Acids Res.* **41**, (2013).

69. Rao, S. S. P. *et al.* A 3D Map of the Human Genome at Kilobase Resolution Reveals Principles of Chromatin Looping. *Cell* **159**, 1665–1680 (2014).

70. Mermel, C. H. *et al.* GISTIC2.0 facilitates sensitive and confident localization of the targets of focal somatic copy-number alteration in human cancers. *Genome Biol.* **12**, R41 (2011).

71. Cheng, S.-W. G. *et al.* Interaction of cyclin-dependent kinase 12/CrkRS with cyclin K1 is required for the phosphorylation of the C-terminal domain of RNA polymerase II. *Mol. Cell. Biol.* **32**, 4691–4704 (2012).

72. O'Leary, P. C. *et al.* Resistance to ATR Inhibitors Is Mediated by Loss of the Nonsense-Mediated Decay Factor UPF2. *Cancer Res.* **82**, 3950–3961 (2022).

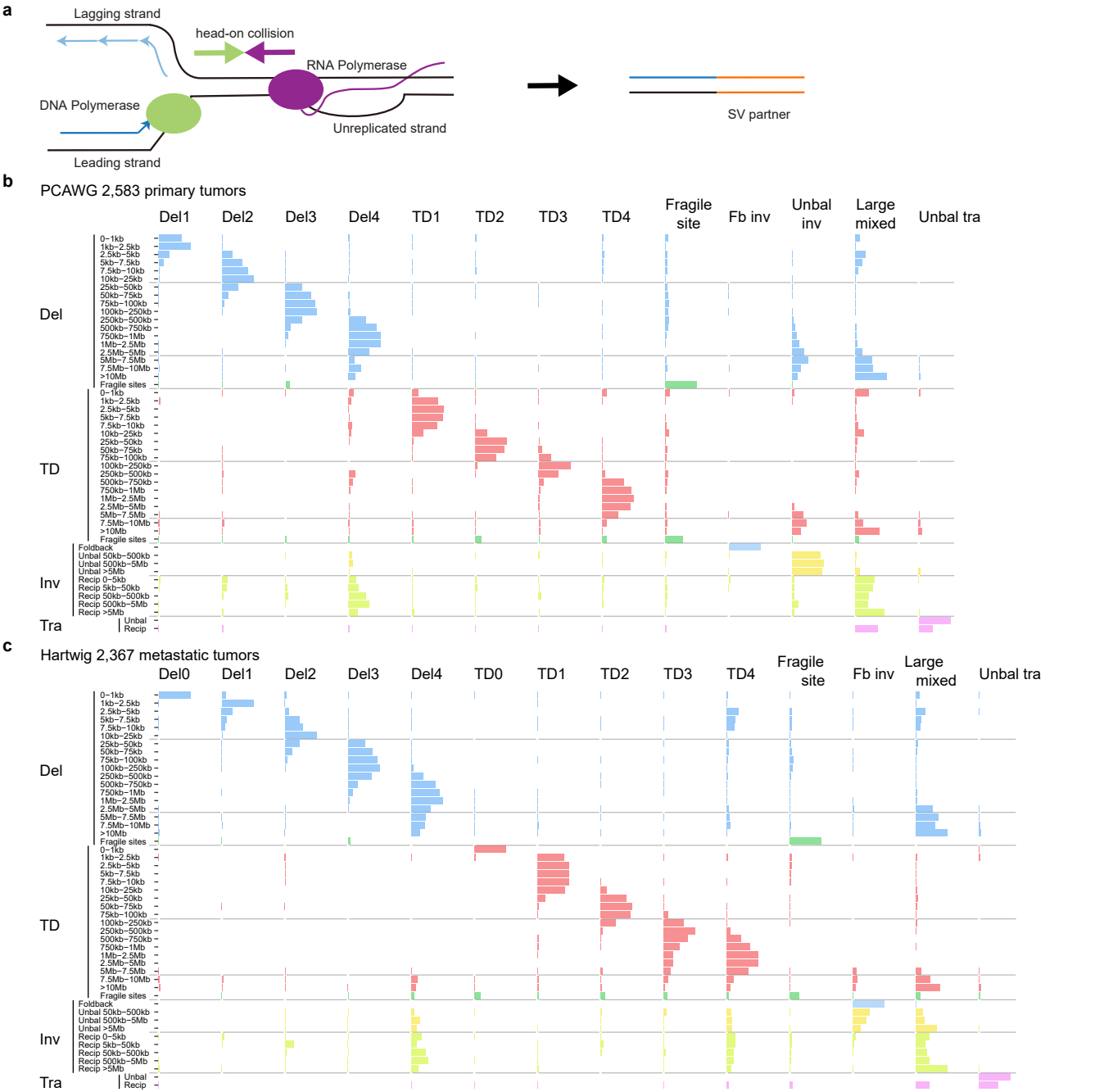
a
Lagging strand
head-on collision
RNA Polymerase
DNA Polymerase
Unreplicated strand
Leading strand
SV partner
b
PCAWG 2,583 primary tumors
Del1
Del2
Del3
Del4
TD1
TD2
TD3
TD4
Fragile site
Fb inv
Unbal inv
Large mixed
Unbal tra
Del
TD
Inv
Tra
0–1kb
1kb–2.5kb
2.5kb–5kb
5kb–7.5kb
7.5kb–10kb
10kb–25kb
25kb–50kb
50kb–75kb
75kb–100kb
100kb–250kb
250kb–500kb
500kb–750kb
750kb–1Mb
1Mb–2.5Mb
2.5Mb–5Mb
5Mb–7.5Mb
7.5Mb–10Mb
>10Mb
Fragile sites
Foldback
Unbal 50kb–500kb
Unbal 500kb–5Mb
Unbal >5Mb
Recip 0–5kb
Recip 5kb–50kb
Recip 50kb–500kb
Recip 500kb–5Mb
Recip >5Mb
Unbal
Recip
c
Hartwig 2,367 metastatic tumors
Del0
Del1
Del2
Del3
Del4
TD0
TD1
TD2
TD3
TD4
Fragile site
Fb inv
Large mixed
Unbal tra
Del
TD
Inv
Tra
0–1kb
1kb–2.5kb
2.5kb–5kb
5kb–7.5kb
7.5kb–10kb
10kb–25kb
25kb–50kb
50kb–75kb
75kb–100kb
100kb–250kb
250kb–500kb
500kb–750kb
750kb–1Mb
1Mb–2.5Mb
2.5Mb–5Mb
5Mb–7.5Mb
7.5Mb–10Mb
>10Mb
Fragile sites
Foldback
Unbal 50kb–500kb
Unbal 500kb–5Mb
Unbal >5Mb
Recip 0–5kb
Recip 5kb–50kb
Recip 50kb–500kb
Recip 500kb–5Mb
Recip >5Mb
Unbal
Recip

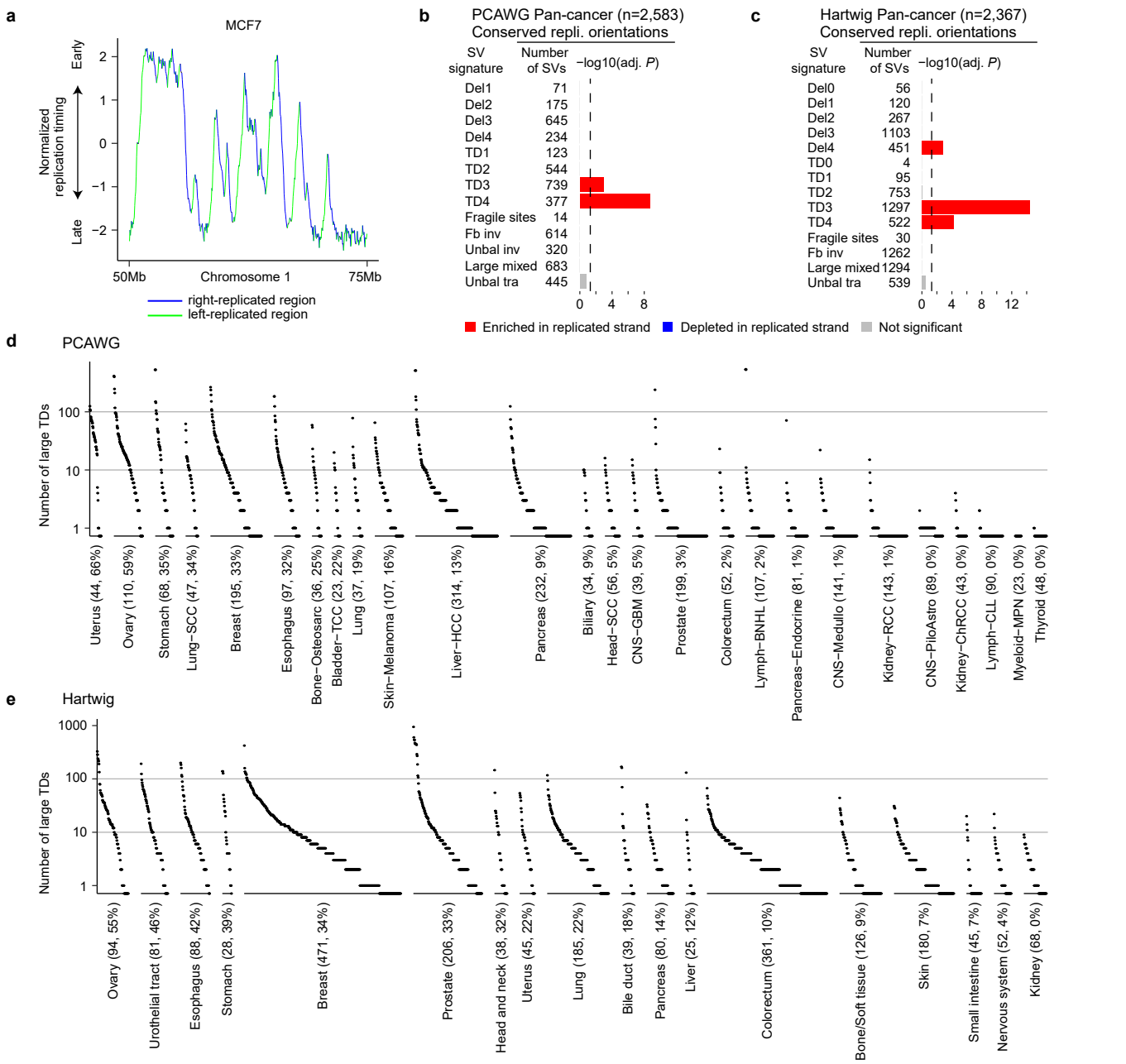
a
MCF7
Normalized replication timing
Early
Late
2
1
0
−1
−2
50Mb
Chromosome 1
75Mb
right-replicated region
left-replicated region
b
PCAWG Pan-cancer (n=2,583)
Conserved repli. orientations
SV signature
Number of SVs
−log10(adj. P)
Del1 71
Del2 175
Del3 645
Del4 234
TD1 123
TD2 544
TD3 739
TD4 377
Fragile sites 14
Fb inv 614
Unbal inv 320
Large mixed 683
Unbal tra 445
0 4 8
c
Hartwig Pan-cancer (n=2,367)
Conserved repli. orientations
SV signature
Number of SVs
−log10(adj. P)
Del0 56
Del1 120
Del2 267
Del3 1103
Del4 451
TD0 4
TD1 95
TD2 753
TD3 1297
TD4 522
Fragile sites 30
Fb inv 1262
Large mixed 1294
Unbal tra 539
0 4 8 12
Enriched in replicated strand
Depleted in replicated strand
Not significant
d
PCAWG
Number of large TDs
100
10
1
Uterus (44, 66%)
Ovary (110, 59%)
Stomach (68, 35%)
Lung−SCC (47, 34%)
Breast (195, 33%)
Esophagus (97, 32%)
Bone−Osteosarc (36, 25%)
Bladder−TCC (23, 22%)
Lung (37, 19%)
Skin−Melanoma (107, 16%)
Liver−HCC (314, 13%)
Pancreas (232, 9%)
Biliary (34, 9%)
Head−SCC (56, 5%)
CNS−GBM (39, 5%)
Prostate (199, 3%)
Colorectum (52, 2%)
Lymph−BNHL (107, 2%)
Pancreas−Endocrine (81, 1%)
CNS−Medullo (141, 1%)
Kidney−RCC (143, 1%)
CNS−PiloAstro (89, 0%)
Kidney−ChRCC (43, 0%)
Lymph−CLL (90, 0%)
Myeloid−MPN (23, 0%)
Thyroid (48, 0%)
e
Hartwig
Number of large TDs
1000
100
10
1
Ovary (94, 55%)
Urothelial tract (81, 46%)
Esophagus (88, 42%)
Stomach (28, 39%)
Breast (471, 34%)
Prostate (206, 33%)
Head and neck (38, 32%)
Uterus (45, 22%)
Lung (185, 22%)
Bile duct (39, 18%)
Pancreas (80, 14%)
Liver (25, 12%)
Colorectum (361, 10%)
Bone/Soft tissue (126, 9%)
Skin (180, 7%)
Small intestine (45, 7%)
Nervous system (52, 4%)
Kidney (68, 0%)

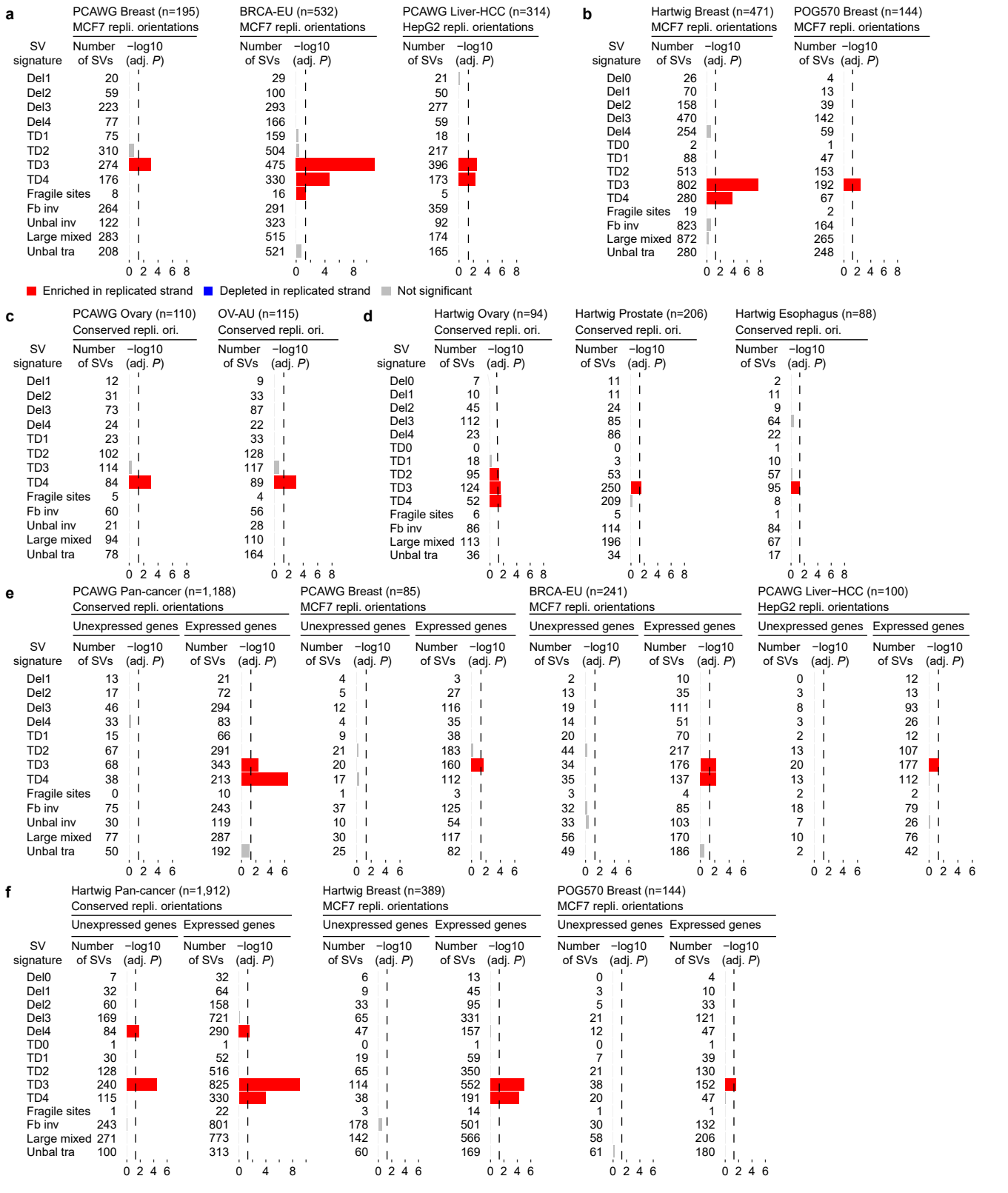
a
PCAWG Breast (n=195)
MCF7 repli. orientations
BRCA-EU (n=532)
MCF7 repli. orientations
PCAWG Liver-HCC (n=314)
HepG2 repli. orientations
b
Hartwig Breast (n=471)
MCF7 repli. orientations
POG570 Breast (n=144)
MCF7 repli. orientations
SV signature
Number of SVs
−log10 (adj. P)
Enriched in replicated strand
Depleted in replicated strand
Not significant
c
PCAWG Ovary (n=110)
Conserved repli. ori.
OV-AU (n=115)
Conserved repli. ori.
d
Hartwig Ovary (n=94)
Conserved repli. ori.
Hartwig Prostate (n=206)
Conserved repli. ori.
Hartwig Esophagus (n=88)
Conserved repli. ori.
e
PCAWG Pan-cancer (n=1,188)
Conserved repli. orientations
PCAWG Breast (n=85)
MCF7 repli. orientations
BRCA-EU (n=241)
MCF7 repli. orientations
PCAWG Liver−HCC (n=100)
HepG2 repli. orientations
Unexpressed genes
Expressed genes
f
Hartwig Pan-cancer (n=1,912)
Conserved repli. orientations
Hartwig Breast (n=389)
MCF7 repli. orientations
POG570 Breast (n=144)
MCF7 repli. orientations

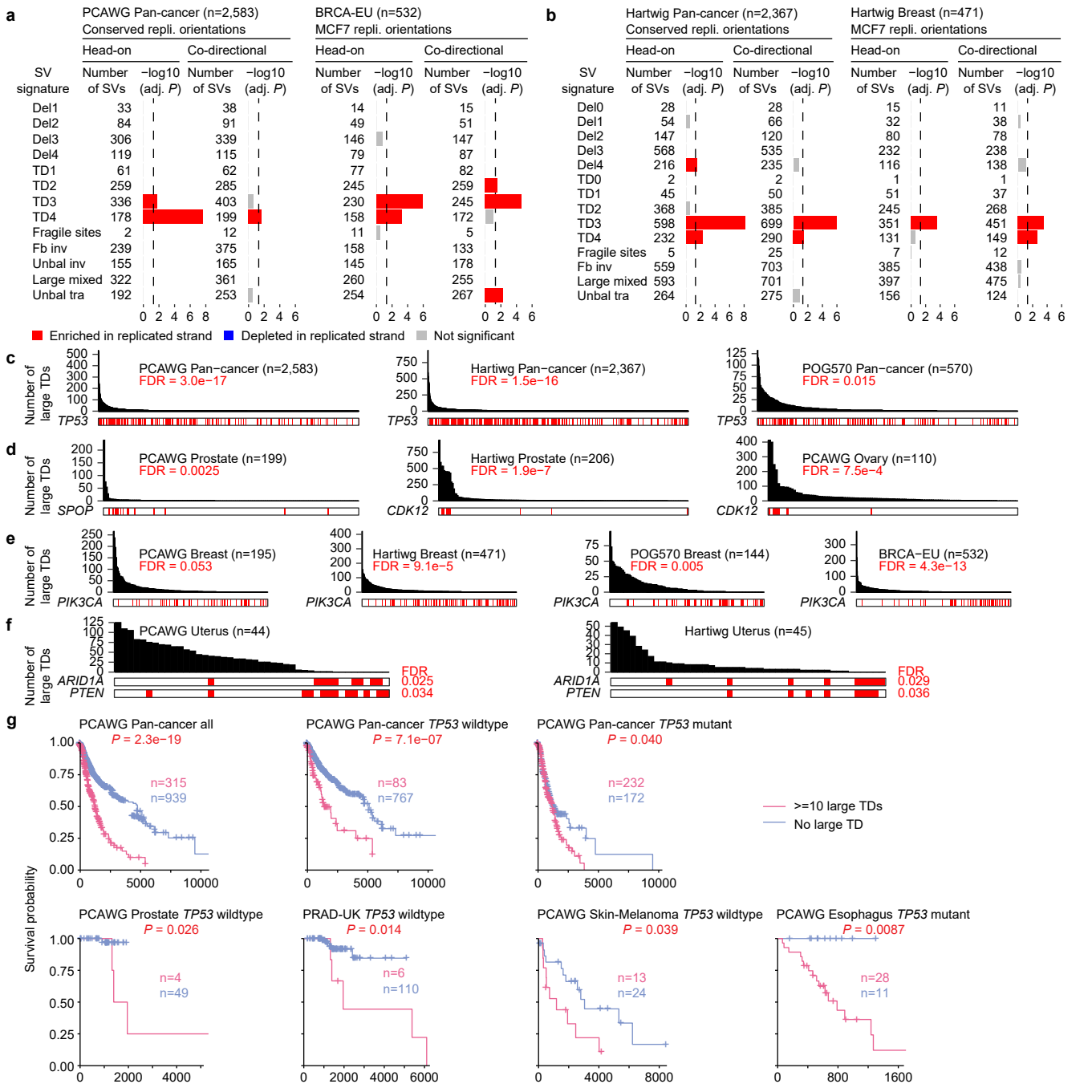
a
PCAWG Pan-cancer (n=2,583)
Conserved repli. orientations
BRCA-EU (n=532)
MCF7 repli. orientations
Head-on
Co-directional
SV signature
Number of SVs
−log10 (adj. P)
Del1 33 38 14 15
Del2 84 91 49 51
Del3 306 339 146 147
Del4 119 115 79 87
TD1 61 62 77 82
TD2 259 285 245 259
TD3 336 403 230 245
TD4 178 199 158 172
Fragile sites 2 12 11 5
Fb inv 239 375 158 133
Unbal inv 155 165 145 178
Large mixed 322 361 260 255
Unbal tra 192 253 254 267
b
Hartwig Pan-cancer (n=2,367)
Conserved repli. orientations
Hartwig Breast (n=471)
MCF7 repli. orientations
Del0 28 28 15 11
Del1 54 66 32 38
Del2 147 120 80 78
Del3 568 535 232 238
Del4 216 235 116 138
TD0 2 2 1 1
TD1 45 50 51 37
TD2 368 385 245 268
TD3 598 699 351 451
TD4 232 290 131 149
Fragile sites 5 25 7 12
Fb inv 559 703 385 438
Large mixed 593 701 397 475
Unbal tra 264 275 156 124
Enriched in replicated strand
Depleted in replicated strand
Not significant
c
Number of large TDs
PCAWG Pan−cancer (n=2,583)
FDR = 3.0e−17
Hartiwg Pan−cancer (n=2,367)
FDR = 1.5e−16
POG570 Pan−cancer (n=570)
FDR = 0.015
TP53
d
PCAWG Prostate (n=199)
FDR = 0.0025
Hartiwg Prostate (n=206)
FDR = 1.9e−7
PCAWG Ovary (n=110)
FDR = 7.5e−4
SPOP
CDK12
e
PCAWG Breast (n=195)
FDR = 0.053
Hartiwg Breast (n=471)
FDR = 9.1e−5
POG570 Breast (n=144)
FDR = 0.005
BRCA−EU (n=532)
FDR = 4.3e−13
PIK3CA
f
PCAWG Uterus (n=44)
Hartiwg Uterus (n=45)
FDR
ARID1A 0.025 0.029
PTEN 0.034 0.036
g
PCAWG Pan-cancer all
P = 2.3e−19
n=315
n=939
PCAWG Pan-cancer TP53 wildtype
P = 7.1e−07
n=83
n=767
PCAWG Pan-cancer TP53 mutant
P = 0.040
n=232
n=172
>=10 large TDs
No large TD
Survival probability
PCAWG Prostate TP53 wildtype
P = 0.026
n=4
n=49
PRAD-UK TP53 wildtype
P = 0.014
n=6
n=110
PCAWG Skin-Melanoma TP53 wildtype
P = 0.039
n=13
n=24
PCAWG Esophagus TP53 mutant
P = 0.0087
n=28
n=11

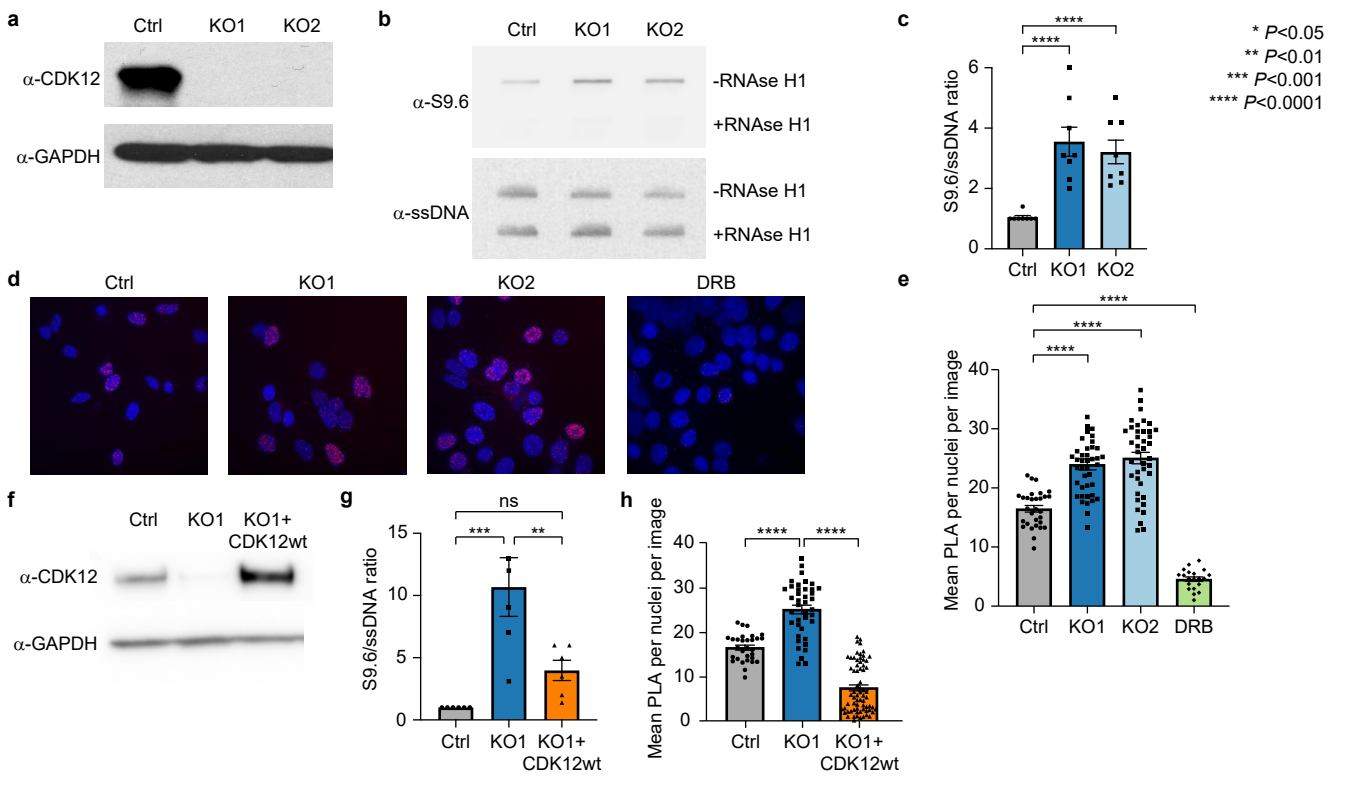
a
Ctrl
KO1
KO2
α-CDK12
α-GAPDH
b
Ctrl
KO1
KO2
α-S9.6
-RNAse H1
+RNAse H1
α-ssDNA
-RNAse H1
+RNAse H1
c
S9.6/ssDNA ratio
Ctrl
KO1
KO2
* P<0.05
** P<0.01
*** P<0.001
**** P<0.0001
d
Ctrl
KO1
KO2
DRB
e
Mean PLA per nuclei per image
Ctrl
KO1
KO2
DRB
f
Ctrl
KO1
KO1+ CDK12wt
α-CDK12
α-GAPDH
g
S9.6/ssDNA ratio
ns
Ctrl
KO1
KO1+ CDK12wt
h
Mean PLA per nuclei per image
Ctrl
KO1
KO1+ CDK12wt

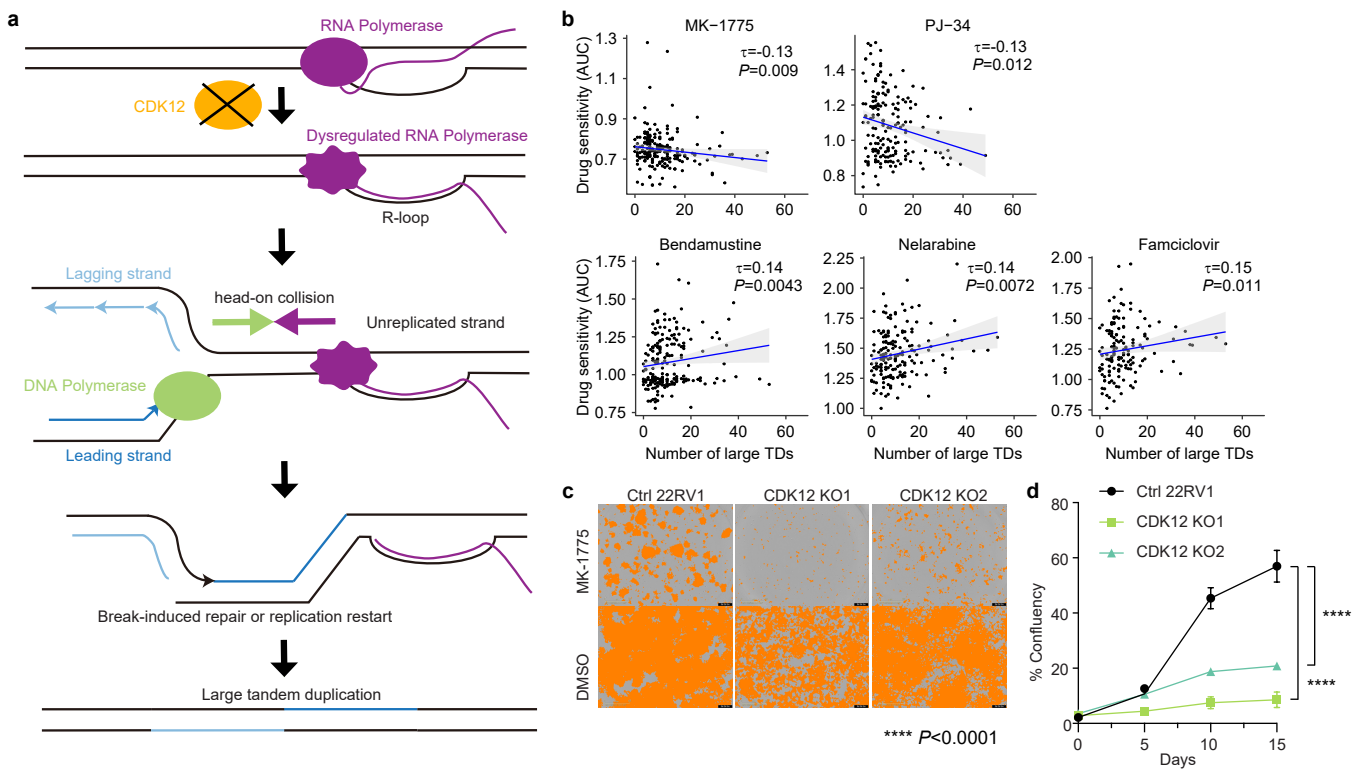
a
RNA Polymerase
CDK12
Dysregulated RNA Polymerase
R-loop
Lagging strand
head-on collision
Unreplicated strand
DNA Polymerase
Leading strand
Break-induced repair or replication restart
Large tandem duplication
b
MK−1775
τ=-0.13
P=0.009
PJ−34
τ=-0.13
P=0.012
Bendamustine
τ=0.14
P=0.0043
Nelarabine
τ=0.14
P=0.0072
Famciclovir
τ=0.15
P=0.011
Drug sensitivity (AUC)
Number of large TDs
c
Ctrl 22RV1
CDK12 KO1
CDK12 KO2
MK-1775
DMSO
**** P<0.0001
d
Ctrl 22RV1
CDK12 KO1
CDK12 KO2
% Confluency
Days
****
****